This Work has not yet been peer-reviewed and is provided by the contributing Author(s) as a means to ensure timely dissemination of scholarly and technical Work on a noncommercial basis. Copyright and all rights therein are maintained by the Author(s) or by other copyright owners. It is understood that all persons copying this information will adhere to the terms and constraints invoked by each Author's copyright. This Work may not be reposted without explicit permission of the copyright owner. This work has been submitted to the Journal of Physical Oceanography. Copyright in this work may be transferred without further notice.

Submesoscale dynamics of dense overflows.

Part II: Near-inertial wave trapping and reflection

Victoria Whitley,[a] Jacob Wenegrat,[a,b] and Leif Thomas[c]

[a] *Applied Mathematics & Statistics, and Scientific Computation Program, University of Maryland, College Park*

[b] *Department of Atmospheric and Oceanic Science, University of Maryland, College Park*

[c] *Department of Earth System Science, Stanford University*

Corresponding author: Victoria Whitley, vicwhit28@gmail.com

ABSTRACT: Near-inertial waves (NIWs) are energetic at high latitudes, yet their interactions with the strongly baroclinic flows of the dense overflows that ventilate the deep ocean have received little attention. Combining linear ray tracing and spectral analysis with a three-dimensional large-eddy simulation of an idealized dense overflow, we examine how the background flow and potential vorticity (PV) structure of a deep boundary current govern the propagation, reflection, and breaking of NIWs. Despite the surface cooling, the descent of gravity currents along the bottom results in layered high-PV bands capping the dense overflow and a wedge of high PV at the shelf break (discussed in Part I of this series). Here we show these high PV features modify the minimum allowable wave frequency and determine where NIWs may travel. Ray tracing shows that waves guided along the sloping isopycnals reflect off high-PV features on the slope and descend into slantwise critical layers along the topography. Power spectra confirm enhanced near-inertial dissipation at these reflection and trapping sites. This study focuses only on the waves generated by this idealized overflow, but the mechanism implies that storm- and tide-forced NIWs of real overflows can enhance mixing and water-mass transformation along deep boundary currents wherever a comparable PV structure arises.

1. Introduction

Mixing near sloping topography is a leading term in the ocean's buoyancy budget, sustaining the diapycnal fluxes that transform abyssal water masses and help close the deep overturning circulation (Polzin et al. 1997; Kunze et al. 2012; Ferrari et al. 2016). Internal waves supply much of the energy for this mixing, with one of the dominant contributions coming from near-inertial waves (NIWs) (Alford et al. 2016). Strong, energetic surface winds are a major source of near inertial kinetic energy both in deep water formation regions and along the path of deep boundary currents (Alford et al. 2016; Kunze et al. 2023; Voet et al. 2024). Likewise, the semidiurnal tide is near-inertial at these high latitudes, further reinforcing the NIW field (Kunze et al. 2023; Voet et al. 2024). Where this energy is ultimately dissipated can contribute to the transformation of overflow waters along the slope, a process that remains difficult to observe directly and to represent in large-scale models (Legg et al. 2009; Magaldi and Haine 2015).

The reflection and breaking of internal waves have often been studied as one way to drive enhanced mixing near topography, with a particularly large focus on the role of critical reflection (Eriksen 1985; Slinn and Riley 1998; Kunze et al. 2012; Chalamalla et al. 2013; Whitley and Wenegrat 2025). In this case, when a wave is propagating at an angle close to that of the slope of the topography the reflected wave becomes trapped with all of its energy concentrated along the boundary (Eriksen 1985; Nokes and Ivey 1989). Most work on this route has concerned the internal tide (Buijsman et al. 2026), whose propagation angle often coincides with the incline of continental slopes (Lamb 2014). For NIWs, in a uniformly stratified ocean, their energy travels at a very shallow angle to the horizontal, reaching critical reflection only along the gentlest slopes (Eriksen 1985; Alford et al. 2016).

However, in a baroclinic, geostrophically balanced current, the properties and propagation of internal waves are modified, and so too are the conditions for critical reflection. The minimum frequency an internal wave can take is a function of the potential vorticity (PV) of the flow (Whitt and Thomas 2013). The canonical lower bound on internal-wave frequency, the Coriolis frequency f, assumes planetary PV, fN^2, where N^2 is the vertical stratification. Yet, in regions where a current enhances PV relative to its planetary value, the minimum frequency becomes superinertial. Where the PV is lowered, such as in regions of anticyclonic vorticity or strong thermal wind shear, a subinertial frequency band opens (Mooers 1975). In all cases, NIWs at the local minimum

frequency propagate along isopycnals. Along dense overflows, where the isopycnals blanket the topography (Girton and Sanford 2003; Magaldi et al. 2011; Spall et al. 2019), this can result in NIWs propagating at much larger angles to the horizontal than are usually considered (Whitt and Thomas 2013; Qu et al. 2021b). The reflection of these waves as they propagate towards regions with a minimum frequency higher than their own can drive enhanced dissipation and mixing (Whitt and Thomas 2013; Qu et al. 2021b). This process is especially important when isopycnals run parallel to bottom topography, allowing for NIWs to be trapped and their energy amplified in slantwise critical layers (Mooers 1975; Kunze 1985; Whitt and Thomas 2013; Qu et al. 2021b). Such interactions have been identified as an efficient route to boundary mixing in other regions with geometry similar to the baroclinic flows and slope-aligned isopycnals found along dense overflows (Qu et al. 2021b,a, 2022).

A companion paper (Whitley et al. 2026) shows that dense overflows shape more than the tilt of their isopycnals. The descending gravity current and subsequent frontal adjustment generate high-PV features that will modify the propagation of any incoming waves. This same region hosts strong shear bands aligned with the isopycnals (Yankovsky and Legg 2019; Whitley et al. 2026). These bands have previously been interpreted in similar simulations as the signature of symmetric instability (SI) (Yankovsky and Legg 2019), but the high PV in the interior rules out SI here. The present analysis supplies an alternative explanation. The banded shear is the signature of NIWs whose propagation is modified by the strongly baroclinic flow of the deep boundary current.

We use the same large-eddy simulation (LES) as in Whitley et al. (2026) to focus on the interaction between NIWs and the baroclinic dense overflow circulation. Section 2 summarizes the numerical configuration, followed by a description of the background flow, PV, and high-frequency variability in section 3. Section 4 briefly reviews the theory governing NIW propagation through a baroclinic mean flow, which is then applied to the simulated overflow in section 5 using ray tracing. Section 6 then uses spectral analysis to establish the frequency content of the banded shear and to locate where the waves reflect, become trapped, and dissipate. Section 7 discusses the implications and summarizes conclusions.

2. Numerical Set Up

The numerical solutions analyzed here come from the same three-dimensional LES presented in the companion paper (Whitley et al. 2026), hence only the elements that bear most directly on wave propagation will be restated. The non-hydrostatic Boussinesq equations are integrated with the Oceananigans package (Wagner et al. 2025) over a domain spanning 8 km across the slope (x) and 300 m in depth, at a resolution of 4 m horizontally and 2 m vertically. The along-slope direction (y) is narrow (150 m) and periodic. This quasi-two-dimensional setup is wide enough for fully three-dimensional turbulence but suppresses baroclinic instability, which could alter the structure of the flow (Smith 1976; Whitehead et al. 1990). The topography is represented as a hyperbolic-tangent slope starting from a 40-m shelf to the full depth of 300 m, with a 1500 m sponge layer on the offshore boundary (in x) absorbing outgoing motions. The Coriolis frequency, $f = 1.43 \times 10^{-4}$ s^{-1}, and the initial stratification, $N_0^2 = 4 \times 10^{-7}$ s^{-2}, are representative of the Denmark Strait (Yankovsky and Legg 2019). The results presented here have been found to be robust to changes in stratification and slope configuration through a set of secondary simulations (Whitley et al. 2026). A steady surface buoyancy loss over the shelf, equivalent to a heat flux of 500 W m^{-2}, generates the overflow. The surface is cooled for 40 inertial periods ($T_f \approx 12.2$ h), and the cooling is then withdrawn over the following five. The run then continues to $80T_f$ without any surface cooling. Unless noted otherwise, the wave analysis draws on this later, quasi-steady stage, after the gravity current has largely spun down and the near-inertial field it excited propagates through the adjusted background.

3. Background state and wave field

The simulation can be split into two stages: the period of active surface cooling above the shelf, and after the cooling has ceased. During cooling (0 – $40T_f$), the dense water formation and resulting gravity currents establish the background flow and stratification that will govern NIW propagation. As the water on the shelf is cooled, large pulses of newly formed dense water escape the shelf in the form of dense gravity currents (green contour, Fig. 1a,b). Each current brings a denser buoyancy class down the slope, building a strongly stratified layer over the deep slope, with isopycnals running parallel to the topography (Fig. 1c) and a bottom-trapped current in geostrophic balance running along the slope (Fig. 1b). Once cooling is shut down (40 – $80T_f$), the gravity

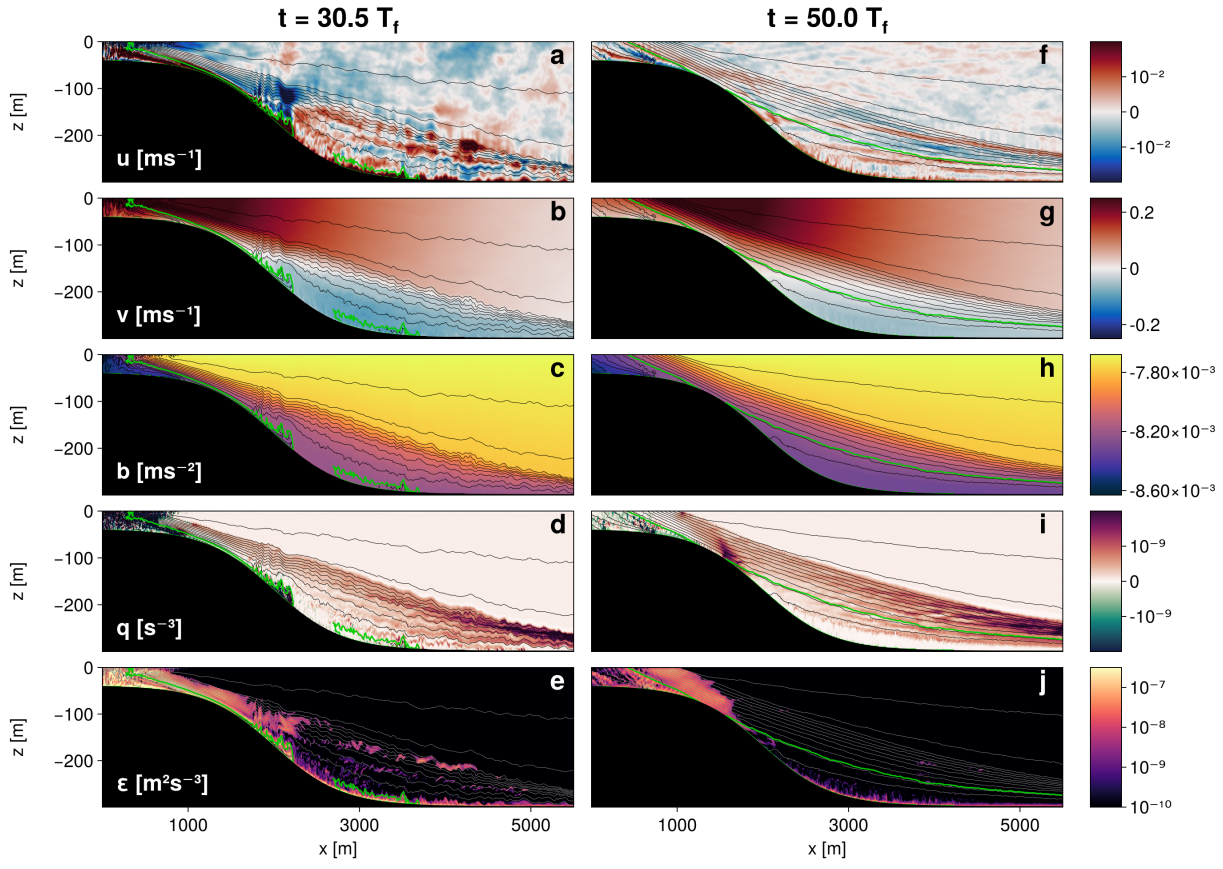
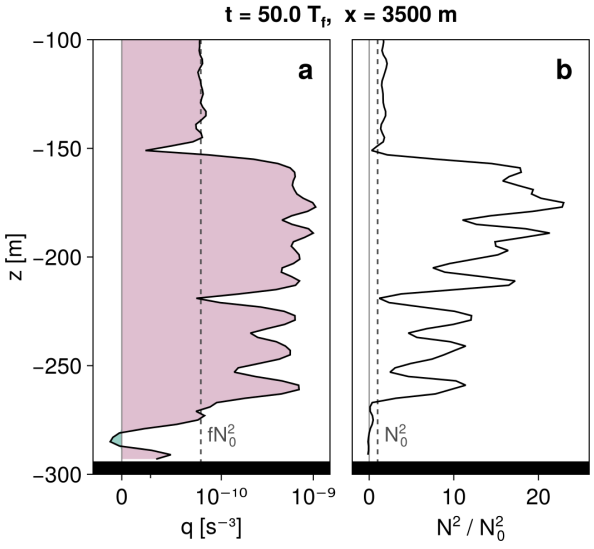


FIG. 1. Snapshots at $t = 30.5T_f$ (surface cooling, a-e) and $50T_f$ (no surface cooling, f-j) of the 3D simulation at $y = 74$ m. Fields shown are the across (a,f) and along-slope (b,g) velocities, u, v, (c,h) buoyancy, (d,i) the Ertel PV, and (e,j) in log scale, the dissipation rate of kinetic energy. Contour lines on all plots are isopycnals at intervals of 5×10^{-5} ms^{-2}. A green isopycnal at -8.22×10^{-3} ms^{-2} marks a passing gravity current during cooling in the first column, and its final location after cooling has shut down in the second. See animations of these fields provided in the supplementary material.

current largely stops, and this adjusted state persists while slowly spinning down for the remainder of the simulation (Fig. 1f-j). This later stage can also be roughly conceptualized as a quasi-Lagrangian view following a segment of the deep boundary current after it leaves its formation region and flows along the slope, with time standing in for distance downstream. Animations of these fields over both stages of the simulation are provided in the supplementary material. The



134 FIG. 2. Vertical profiles at $x = 3500$ m ($y = 74$ m) and $t = 50\ T_f$ of (a) Ertel PV, q, and (b) stratification, N^2,
135 normalized by its initial value, N_0^2. In (a) the horizontal axis in log scale for $|q| > 10^{-11}$ s^{-3} and logarithmic
136 beyond, and shading marks positive (purple) and negative (teal) PV. Dashed lines mark the initial interior values
137 fN_0^2 and N_0^2, and black shading is topography.

128 wave analysis in sections 5 and 6 focuses on this more quiescent stage, but the features that control
129 wave propagation are all generated while the dense overflow is active.

138 Chief among these features is the PV field the overflow leaves behind (Fig. 1i). Here, Ertel PV,
139 q, is calculated as,

$$q = (\boldsymbol{f} + \boldsymbol{\omega}) \cdot \nabla b, \tag{1}$$

140 where $\boldsymbol{f}$ is the Coriolis vector, $\boldsymbol{\omega}$ is the relative vorticity vector, and b is buoyancy. On the shelf,
141 the surface buoyancy loss destroys PV ($x \lesssim 600$ m; Fig. 1d; Whitley et al. 2026), with negative
142 PV remaining on the shelf long after surface cooling has shut off (Fig. 1i). Each gravity current
143 thus starts with negative PV, but as it flows down along the bottom topography near the shelf break
144 ($x = 800 - 2000$ m, Fig. 1d) it gains PV due to the frictional injection associated with the bottom
145 stress exerted by the current along the topography (Whitley et al. 2026). The dense overflow
146 waters thus carry a *high* PV anomaly into the interior strongly stratified region. The injection
147 event associated with each passing current creates a layered history of high PV capping the dense

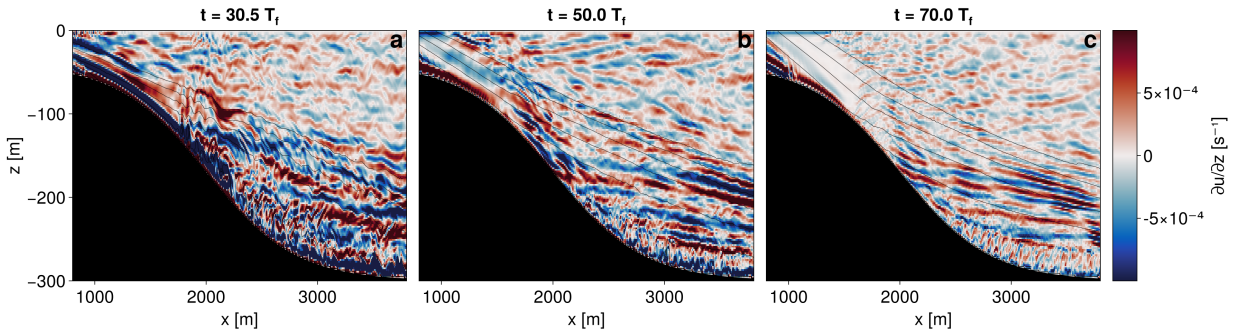


FIG. 3. Snapshots of vertical across-slope shear, $\partial u/\partial z$, at (a) $t = 30.5T_f$, (b) $50.0T_f$, and (c) $70.0T_f$ show the internal waves generated by the overflow propagating through the domain, with buoyancy- and topography-aligned banded structures in the strongly stratified interior ($z < -200$ m). Thin black contours in all panels denote isopycnals corresponding to evenly spaced buoyancy classes.

overflow in the deepest part of the domain ($x > 4000$ m, Fig. 1d). A representative vertical profile at $x = 3500$ m of PV and the stratification N^2 shows this banded structure in the interior near the bottom, with high PV reaching 10^{-9} s^{-3} in magnitude (Fig. 2a). In between the layers, the PV is much smaller, closer to the initial background PV of the system, fN_0^2. Besides a small bottom boundary layer ($z \lesssim -280$ m), the PV is consistently positive (Fig. 2a). Once the cooling ends, frictional surface fluxes during the adjustment of the shelf-break front deposit additional PV just past the shelf break ($x = 1500 - 2000$ m, Fig. 1i). This 'wedge' of accumulated high PV at the shelf break, along with the layered capping in the interior and the negative PV left on the shelf, will modify the propagation of any waves generated by the overflow. The formation of this PV structure—critical to the dynamics explored here—is examined in detail in the companion paper (Whitley et al. 2026).

The overflow is also a source of internal waves. While the cooling is active, turbulence on the shelf and the periodic turbulent gravity currents descending the slope continually excite waves that fill the interior (Fig. 3a). Once the forcing is withdrawn, the waves propagate through the adjusted background and slowly decay (Fig. 3b,c). In the weakly stratified upper interior, beams of internal wave energy trace the classic "St. Andrew's cross" ($z > -100$ m, Fig. 3b,c). In the more highly stratified interior below, the shear instead organizes into thin, slantwise bands, tilted to follow the isopycnals and the topography beneath them and confined to the same high-PV stratified layer

($z < -200$ m, Fig. 3b,c). Both structures stand out more sharply as the overflow spins down and the gravity current and associated turbulence fade. The strong shear in this region is accompanied by bands of elevated rates of dissipation of kinetic energy, on the order of 10^{-8} m^{2}s^{-3}, weaker than on the shelf where cooling occurs but well above the interior background (Fig. 1e). The dissipation rate, ϵ, is calculated directly from model fields as,

$$\epsilon = \nu_e \frac{\partial u_i}{\partial x_j} \frac{\partial u_i}{\partial x_j}, \tag{2}$$

where ν_e is the turbulent eddy viscosity, and summation over repeated indices is implied. The magnitude of the dissipation rate decays with time as the overflow spins down (Fig. 1j), and hence should be used here as a proxy for where mixing might occur, not as a measure of its strength in realistic settings.

Similar banded shear structures have been reported in the larger-scale overflow simulations of Yankovsky and Legg (2019), run under comparable forcing but at coarser resolution. Their PV field was also layered, with thin bands of positive PV along the slope separated by bands of negative PV. The shear bands coincided with the negative PV bands and were attributed to SI. The bands in Fig. 3 closely resemble that shear signature, and the layered PV structure is also similar, but the PV remains positive (Fig. 2), as diagnosed in Part I (Whitley et al. 2026). The closest counterparts to their negative PV bands are the thin layers of low, but consistently positive, PV between the high-PV layers here (Figs. 2, 1i). With the interior PV entirely positive, outside a thin bottom boundary layer ($z \lesssim -280$ m, Fig. 4d), the interior remains stable to SI (Thorpe and Rotuno 1989; Taylor and Ferrari 2009).

Here we offer a different dynamical interpretation of these features. Slantwise shear coherent along isopycnals is also the expected signature of NIWs propagating near their minimum frequency through a strongly baroclinic flow (Whitt and Thomas 2013). Similarly tilted shear bands observed in the Straits of Florida after the passage of tropical storms were identified as signatures of storm-generated NIWs, the deepest of which enter a slantwise critical layer over the sloping boundary (Qu et al. 2021a). The remainder of this paper tests whether the same interpretation holds for the bands found here. Section 4 describes how the mean flow and PV structure set where NIWs can propagate, section 5 traces the wave paths through this background, and section 6 returns to the bands to examine their frequency content and the dissipation associated with them.

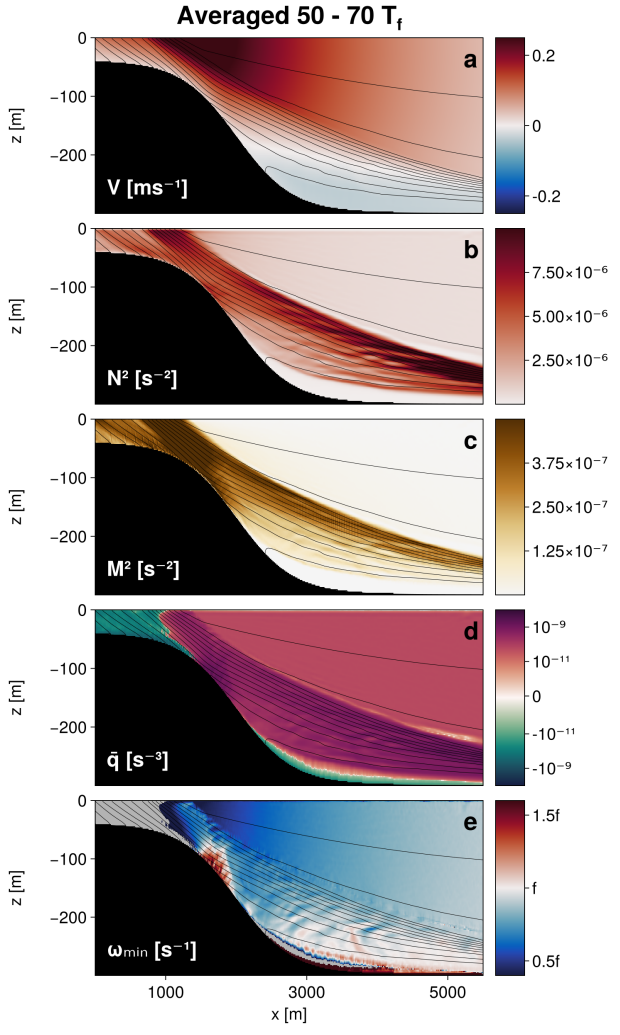


FIG. 4. Long-term averages over $50-70T_f$, after cooling has shut down, of the 3D simulation. (a) along-slope velocity, V, (b) vertical, N^2, and (c) horizontal stratification, M^2, (d) Ertel PV (log scale), and (e) the minimum wave frequency, $\omega_{\min}$ in terms of the local Coriolis frequency, f. Gray regions in (e) represent where the minimum wave frequency takes on an imaginary value. Contour lines on all plots are isopycnals expressed in units of buoyancy at intervals of $5\times10^{-5}\,\mathrm{m\,s^{-2}}$.

4. Near-inertial waves in a baroclinic mean flow

In the classical theory for internal waves in a resting, uniformly stratified ocean, wave frequencies are bounded below by f, and near-inertial energy travels at very shallow angles to the horizontal. In a background state like the one left by the overflow (Fig. 4), neither assumption holds. Instead,

assume waves propagating in (x,z), with a mean background flow, V (Fig. 4a), and mean vertical and horizontal stratification, $N^2 = \partial b/\partial z$ and $M^2 = \partial b/\partial x = f\partial V/\partial z$ (Fig. 4b,c), then the linear hydrostatic dispersion relation becomes

$$\omega^2 = \alpha^2 N^2 + f(f + \frac{\partial V}{\partial x}) - 2M^2\alpha, \tag{3}$$

where $\alpha = k/m$ is the aspect ratio of the wave and (k,m) is its wavevector (Whitt and Thomas 2013). The first two terms on the right-hand side are inherited from the classical limit. The other two carry the imprint of the mean flow, with the vertical vorticity of the balanced current shifting the effective inertial frequency, $\sqrt{f(f+V_x)}$ and the baroclinic term, $-2M^2\alpha$, breaking the symmetry between the two wave characteristics and opening the subinertial frequency band (Mooers 1975; Whitt and Thomas 2013).

The minimum wave frequency is thus given by the frequency of waves propagating along isopycnals, $\alpha_{min} = \frac{M^2}{N^2} = -s_b$ (where s_b is the slope of isopycnals, Whitt and Thomas 2013), which can be written in terms of the mean PV of the background flow, $\bar{q} = (f+V_x)N^2 - M^4/f$,

$$\omega_{\min} = \sqrt{f\bar{q}/N^2}, \tag{4}$$

(Whitt and Thomas 2013). This expression ties the wave physics directly to the PV structure described in section 3. Where PV is enhanced relative to the planetary PV, as in the layered capping near the slope in the interior and the accumulated 'wedge' along the shelf break, the minimum frequency becomes superinertial and waves at or below f cannot propagate (red regions, Fig. 4e). Such regions act as barriers that reflect incoming NIWs (Whitt and Thomas 2013; Qu et al. 2021b). Where PV is reduced relative to fN^2 but still positive, $\omega_{\min}$ falls below f and subinertial waves are permitted (blue regions, Fig. 4e), and where PV is negative, as on the shelf (gray regions, Fig. 4e), $\omega_{\min}$ is imaginary and the flow supports growing motions such as SI rather than propagating waves (Thorpe and Rotuno 1989; Taylor and Ferrari 2009; Whitley et al. 2026).

The theoretical path along which NIW energy would propagate through the background left by the overflow can be modeled using the group velocity of the wave. The rays of energy propagation for a given initial condition can be found by solving the ordinary differential equation determining

the slope of the wave characteristics, λ,

$$\frac{dz^r}{dx^r} = \lambda = s_b \pm \sqrt{\frac{\omega^2 - \omega_{\min}^2}{N^2}} \tag{5}$$

where (x^r,z^r) is the location of the ray (Whitt and Thomas 2013; Qu et al. 2021b). The two characteristics are symmetric about the local isopycnal slope rather than the horizontal, so rays bend as the stratification and PV change along their path, and a ray can even switch between downward and upward energy propagation without reflection (Whitt and Thomas 2013; Qu et al. 2021b). The fate of a ray at the edge of a barrier region depends on the orientation of the boundary where $\omega = \omega_{\min}$ relative to the ray path (Qu et al. 2021b). Where this boundary cuts across the incoming rays, as when a ray runs into a localized region of high PV, the wave reflects at a turning point and its energy is redirected. Where the boundary instead runs parallel to the rays, the wave can neither cross it nor radiate away from it. Both characteristics converge onto the isopycnal slope, the group velocity vanishes, and the wave is trapped and amplified in what is called a slantwise critical layer, as the trapping boundary is aligned with the sloped isopycnals (Kunze 1985; Whitt and Thomas 2013; Qu et al. 2021b). When the overflow generates slope-aligned isopycnals, a critical layer could form directly against the topography and concentrate wave breaking, and any associated mixing, at the boundary (Qu et al. 2021b,a, 2022).

5. Near-inertial wave propagation

Once the background flow is quasi-steady (after cooling has been shut off), the time-averaged fields of Fig. 4 supply the stratification, shear, and PV that enter (3)–(5), and the theoretical paths of NIW energy through the domain can be traced. Ray tracing of an inertial wave, $\omega_0 = 1.0f$, is shown in Fig. 5, with initial locations (black stars) chosen to span the depth of the simulation in the interior (Fig. 5a) and the surface region near the shelf-break front (Fig. 5b). The rays initiated from the interior represent remotely forced waves that propagate towards the slope, whereas those initiated at the front represent nearfield generation arising directly from responses to changing surface forcing or emission during frontal adjustment.

Across-slope velocity shear from the simulated wave field was band-pass filtered to the ray tracing frequency (Fig. 5 c,d). The filtered field shows significant NIW energy persisting long

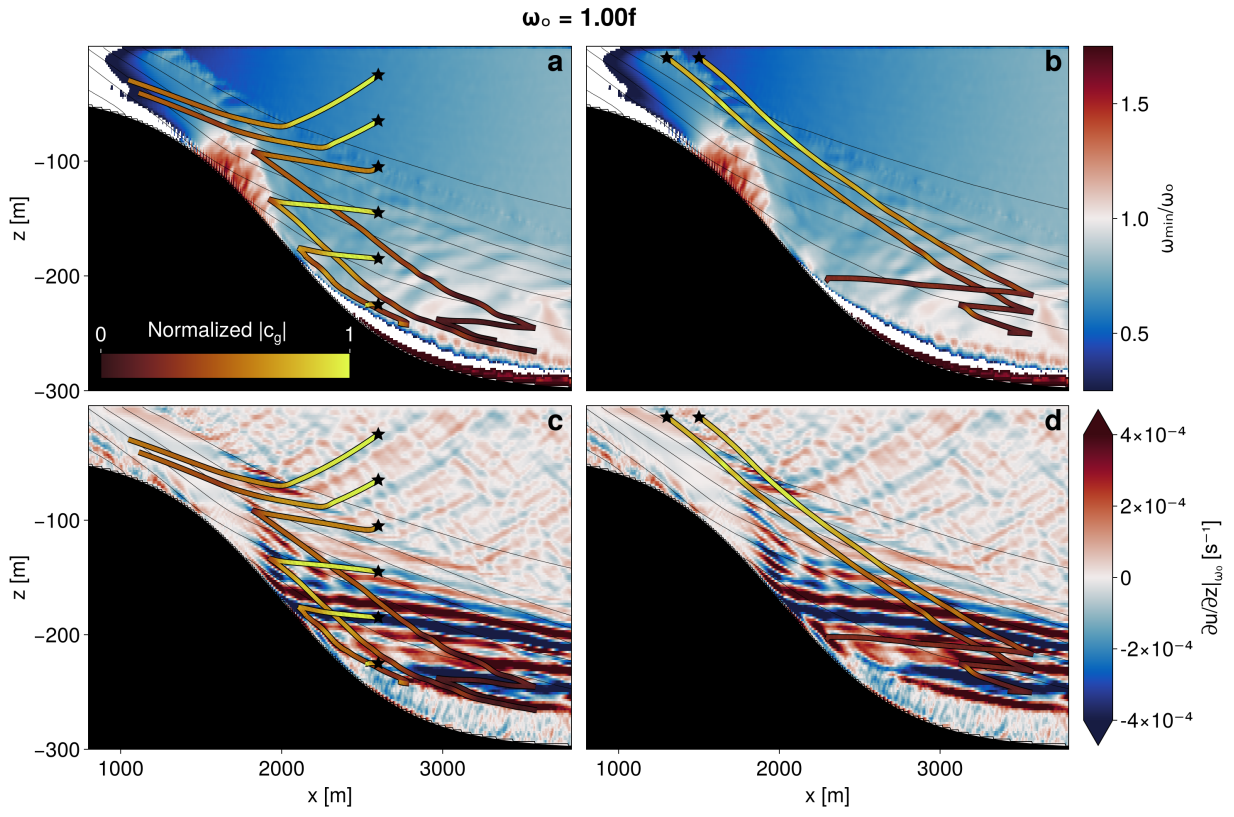


FIG. 5. Ray tracing at a frequency of $\omega_0 = 1.0f$ starting at initial locations given by the black stars, representing both farfield (a,c) and nearfield (b,d) generation sites. The color of the ray is given by the normalized group velocity of that ray. The background in the top row (a,b) is the ratio of the minimum frequency to the ray frequency, averaged over $50-70T_f$. Red regions where the minimum frequency is higher than the ray's indicate how the background flow can modify the propagation of NIWs. (c,d) vertical shear at $t = 60T_f$, with a band-pass filter at the ray tracing frequency, illustrating the agreement of ray tracing with the true wave propagation.

after cooling has shut down. At this frequency, rays originating from the more weakly stratified upper interior ($z > -100$ m) initially propagate downward along the lower characteristic, in the negative z direction. When the rays reach the strongly stratified region, they bend upwards ($\lambda > 0$), still propagating along the ray characteristic that would typically travel downward ($m > 0$) under classical linear theory without modification by the baroclinic background flow ($(x, z) \approx (2200, -80)$ m, Fig. 5a). This counterintuitive upward trajectory is the reversal of vertical energy propagation permitted in a baroclinic mean flow (section 4), arising here from the steep slope of the isopycnals

((5), Whitt and Thomas 2013). Bands of NIWs in the filtered shear snapshots show the bending of these incoming NIWs as they encounter the shelf-break front ($(x, z) \approx (1700, -50)$ m, Fig. 5c).

The fate of these incoming rays depends on their depth relative to the 'wedge' of high PV, and therefore superinertial $\omega_{\min}$, that accumulates at the shelf break (red region, $x = 1500 - 2000$ m, Fig. 5a). Rays from the upper interior ($z > -100$ m) propagate into the shelf-break front, where the bending along the steep isopycnals brings neighboring rays nearly parallel and slows their group velocity, resembling the approach to a slantwise critical layer (Qu et al. 2021b). No such layer forms here, however. Well before the group velocity vanishes, these rays pass into the remnant of negative PV left on the shelf by cooling ($x < 1000$ m), where $\omega_{\min}$ is imaginary and the fate of the upper rays cannot be confirmed from ray tracing (see Whitley et al. 2026, for discussion of symmetric instability on the shelf). Rays originating further down ($z < -100$ m), in the region of slope-aligned isopycnals, follow the same upwards trajectory along the isopycnals until encountering the wedge. The high PV abruptly increases the minimum frequency, causing the rays to reflect off the wedge itself (where $\omega_{\min}$ is superinertial). The rays propagate down toward the interior bottom boundary ($x = 2000 - 2500$ m, Fig. 5a,c). The role of the high PV at the shelf break in blocking incoming NIWs is manifest as greatly reduced vertical shear relative to the shears of the banded wave structures in the interior (Fig. 5c,d).

Rays initialized at the surface along the shelf-break front (Fig. 5b,d) and the interior rays reflected off the high-PV wedge (Fig. 5a,c) both follow the topography-aligned isopycnals into the strongly stratified layer in the deepest part of the domain. The surface-initialized rays mostly reflect off patches of high minimum frequency and are funneled closer to the boundary ($x = 3000$ – 3500 m, Fig. 5b,d), while the rays seeded in the interior, initially spaced 40 m apart, converge after reflection, aligning with the isopycnals that run parallel to the bottom boundary ($x = 2800$ – 3500 m, Fig. 5a,c). As the local $\omega_{\min}$ rises towards the ray frequency, the group velocity tends to zero, and the waves are trapped and amplified in a slantwise critical layer, where increased mixing and dissipation are expected. The bandpassed inertial shear can be seen to be enhanced along the same regions predicted by the wave tracing, supporting the dynamical interpretation offered.

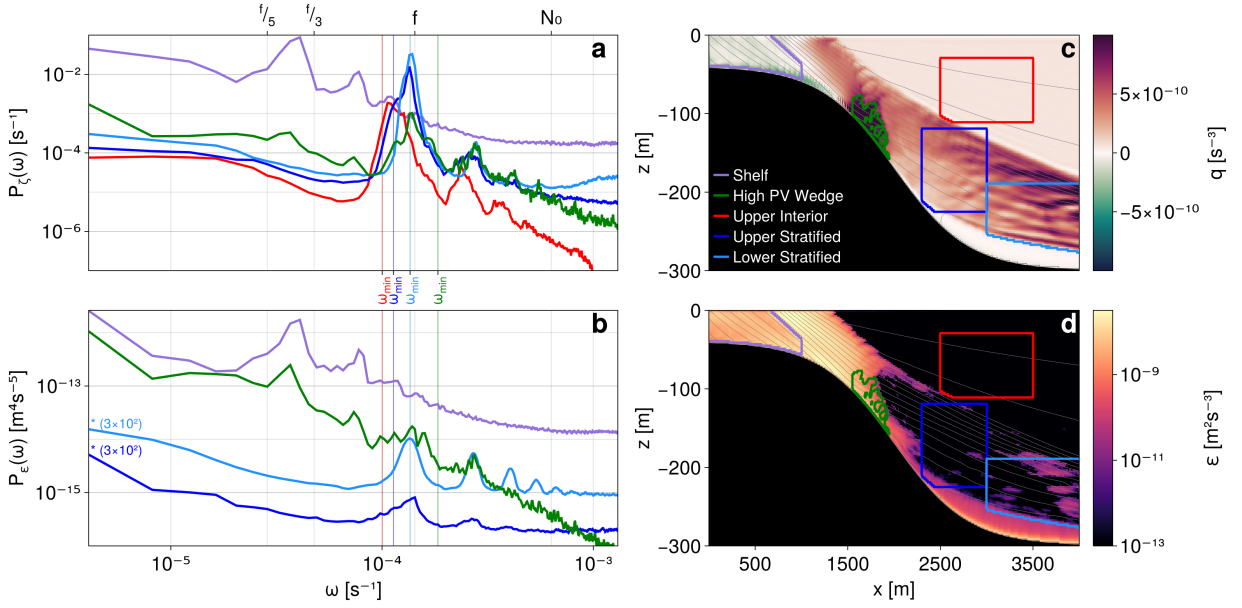


FIG. 6. Power spectra of (a) vertical vorticity and (b) dissipation rate of kinetic energy taken over different regions of interest. The colors of the lines in the spectra match the color of the regions they represent (see legend for naming conventions), marked in the post-cooling, inertially averaged plots of (c) the Ertel PV and (d) the dissipation rate of kinetic energy. Spectra for the dissipation rates in the regions marked "upper and lower stratified" have been multiplied by 300 for clarity in plotting.

6. Near-inertial wave spectra and dissipation

Power spectra of the vertical vorticity (Fig. 6a) confirm that the waves generated by the dense overflow are concentrated in the near-inertial band (as assumed in the ray tracing above). The spectra were computed at all points within each region marked in Fig. 6c,d and then averaged. The labels in the corresponding legend (Fig. 6c) identify the regions referred to throughout the following discussion. Following the convergence approach used to validate LES of gravity wave breaking (Remmler et al. 2015), a second simulation at doubled horizontal and vertical resolution verifies the following spectral results. It confirms that the thinnest shear bands ($\sim$ 16 m) are sufficiently resolved by the baseline grid spacing (Δz = 2 m), satisfying the standard numerical criterion of eight grid points per wavelength for resolving wave-like and stratified fluid structures (Arbic et al. 2010).

The spectral peak in the shelf region (purple lines, Fig. 6a) matches the subinertial frequency of the dense pulses related to SI after cooling shuts down (Whitley et al. 2026). There are no other frequency peaks on the shelf, consistent with the ray tracing above. The negative PV left on the shelf by cooling (Fig. 4d), along with the steep isopycnals from the strong horizontal buoyancy gradient (Fig. 4c), means near-inertial waves could only propagate through this region at angles much steeper than the isopycnals. Due to the negative PV, this region is also symmetrically unstable, and any near-inertial energy that arrives would most likely be overwhelmed by SI (Whitley et al. 2026). The following analysis therefore focuses on the interior, where much of the wave field lies close to the minimum frequency (Fig. 6a).

Within the interior, the spectra differ slightly by region (Fig. 6a). The waves in the upper interior (red lines) have subinertial frequencies, with a peak near $0.74f$, consistent with the lowered minimum frequency there (average ω_{min} marked by the vertical line of matching color in Fig. 6a,b). The upper and lower stratified regions (dark and light blue lines, respectively), sampling the strongly stratified interior at its upslope end and along the bottom, farther downslope, have frequencies closer to inertial, with peaks between $0.94f$ and $1.0f$. These clear near-inertial frequency peaks provide additional evidence that the banded shear signature found along the slope in the interior is propagating NIWs (Figs. 3, 6a). Qualitatively similar features in other simulations of dense water formation have been interpreted as SI due to observed thin bands of negative PV (Yankovsky and Legg 2019), but here the bottom injection of PV keeps the interior stable to SI (Fig. 6c). The bands are instead the signature of the wave field itself.

The subinertial portion of the wave field can be followed with the same ray tracing. Rays with a frequency of $\omega_0 = 0.8f$, initialized at the same locations as the $\omega_0 = 1.0f$ case, show similar initial trajectories to the higher frequency case (Fig. 7). These rays cannot propagate as far into the interior due to the high-PV layer raising the minimum frequency. The rays reflect off the same high-PV feature, as well as interior regions of higher minimum allowable wave frequency, before being funneled down towards the boundary (Fig. 7).

The ray tracing at the frequencies of the observed peaks in the vorticity spectra ($\omega_0 = 0.8f, 1.0f$) predicts the path of wave energy fluxes. Reflected waves converge in the upper stratified region as they are funneled downward, and trapped waves amplify in the slantwise critical layer along the boundary of the lower stratified region. If NIWs are breaking at these sites, the dissipation there

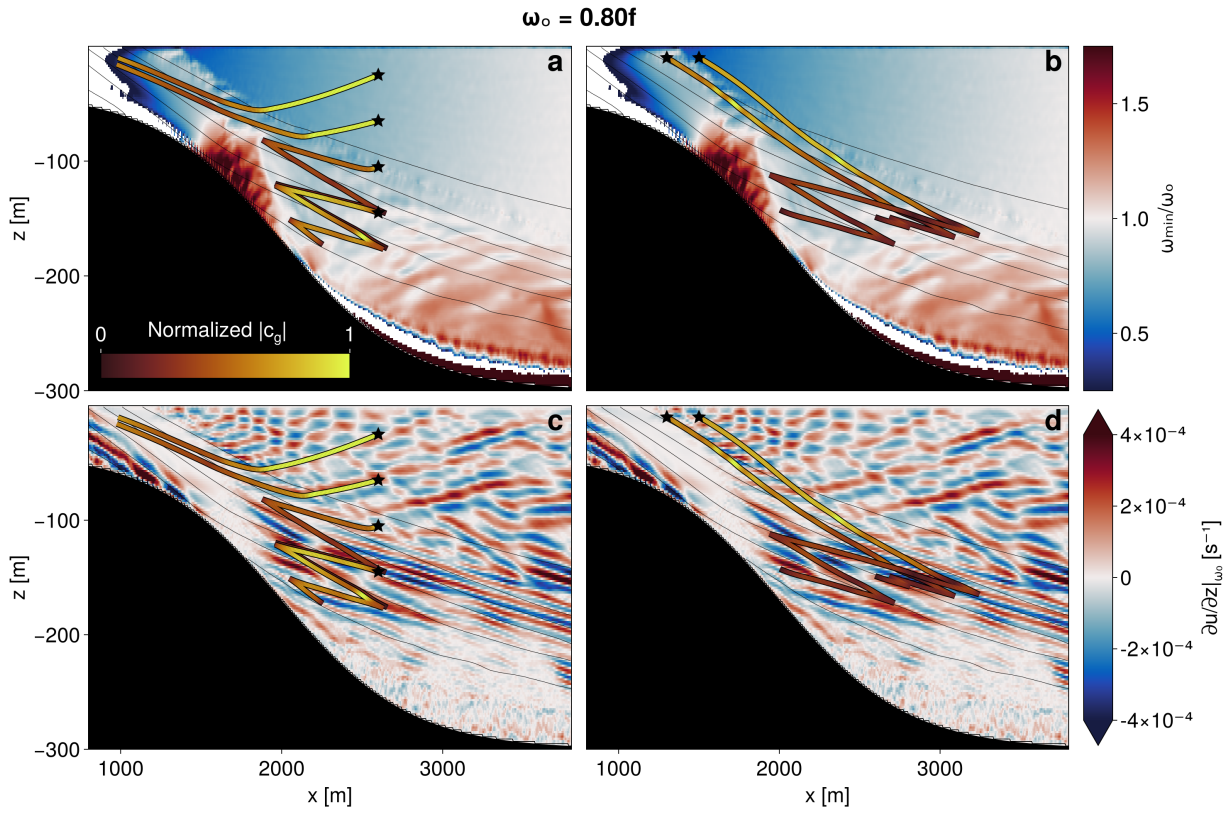


FIG. 7. Ray tracing as in Fig. 5, with rays initialized with a subinertial frequency, $\omega_0 = 0.8f$.

should be organized at near-inertial frequencies, whereas turbulence inherited from the gravity current or the mean flow carries no such signature. To check this, spectra of the dissipation rate of kinetic energy for each region are also shown in Fig. 6b. The interior dissipation rates are much lower than those on the shelf and high-PV wedge, so the spectra from the "upper and lower stratified" regions (blue lines) are multiplied by 300 for visualization, and the upper interior, which shows no discernible peaks, is omitted for clarity. This weak interior signal is expected, as the waves generated during the dense overflow decay quickly once cooling shuts down (Fig. 3b,c). Even so, the interior peaks remain useful indicators of processes that would generate stronger turbulence in a more realistic and energetic background wave field.

Both regions show the expected near-inertial dissipation signal. In the upper stratified region (dark blue line), the dissipation peak matches the vorticity peak, spanning frequencies between the local minimum frequency and the superinertial minimum inside the region where high PV accumulated at the shelf break (Fig. 6b). Waves in this frequency band are exactly those that can

propagate in the upper stratified region but are turned back by the wedge, tying this dissipation to the reflected and funneled waves in the ray tracing (Figs. 5a,c, 7a,c).

The high-PV "wedge" on the slope shows a vorticity peak in the same near-inertial band as the interior (green lines, Fig. 6a, $\omega = 0.94f$), but below the local minimum allowable frequency. This peak is potentially a signature of evanescent waves, a remnant of the NIWs propagating toward and reflecting off this region (Thomas and Wenegrat 2026). The subinertial dissipation on the shelf and within the wedge instead reflects SI and gravity-current dynamics, examined in the companion paper (Whitley et al. 2026). Higher harmonic peaks in both the vorticity and dissipation spectra (Fig. 6a,b) may further reflect wave-wave interactions generated by NIWs that break or radiate away.

The near-inertial organization of the dissipation is clearest in the lower stratified region, however, where the dissipation and vorticity spectra peak together just below f (light blue line, Fig. 6a,b). The dissipation is also elevated along the boundary (Fig. 6d), at the location of the slantwise critical layer in the ray tracing (Fig. 5a,c), confirming that trapped NIWs are enhancing dissipation near the boundary. The spectral peaks therefore indicate that NIW trapping and breaking near the slope can drive additional mixing. Because the critical layer concentrates this dissipation against the boundary, in the stratified layer directly above the densest overflow waters, it is the component of the wave-PV interaction most likely to drive water-mass transformation in a realistically forced overflow.

7. Discussion and conclusions

The results discussed above are summarized in the schematic in Fig. 8, with important regions and processes referenced by the numbers in blue circles. A companion paper (Whitley et al. 2026) established how boundary fluxes of PV shape the interior of this dense overflow: frictional injection beneath the passing gravity current (Fig. 8a, regions 1 and 2) caps the overflow with layered high PV at depth (region 3), while frontal adjustment after cooling builds a "wedge" of accumulated high PV along the bottom at the shelf break (Fig. 8b, regions 4 and 5). Here we focused on how that structure affects the propagation and fate of NIWs. The overflow generates internal waves with near- and sub-inertial frequencies (Fig. 8b, region 6). Raytracing indicates that the baroclinic structure of the deep boundary current guides NIWs from the interior towards the

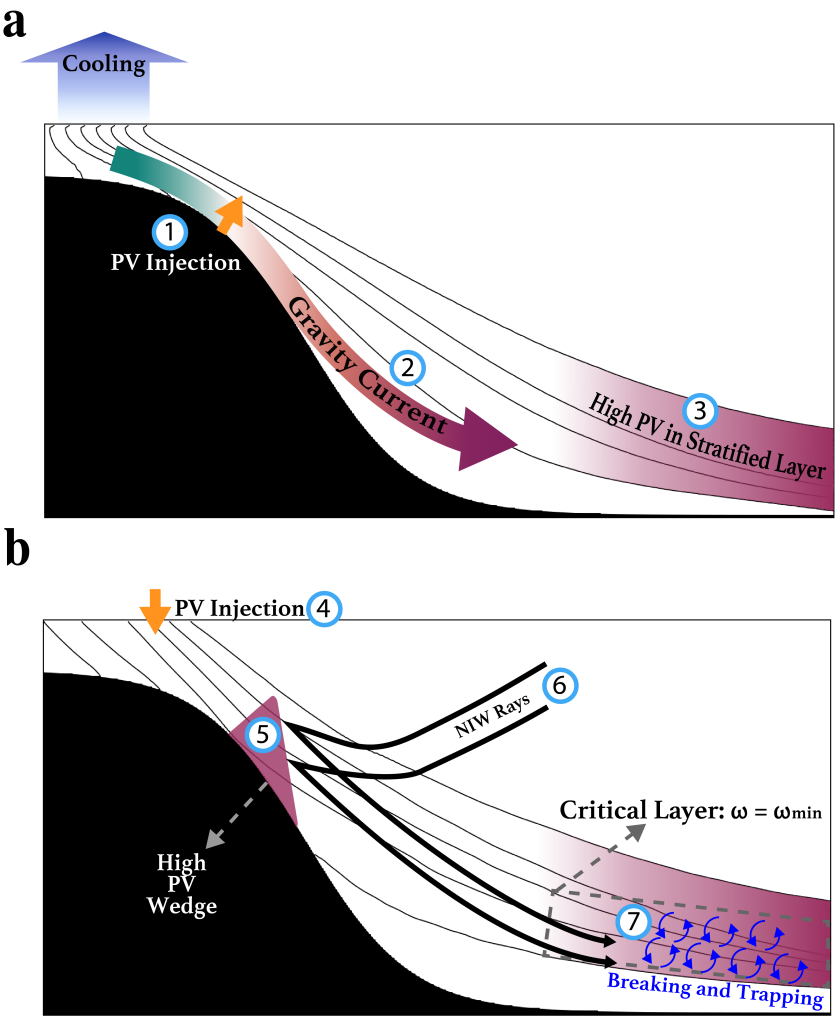


FIG. 8. Schematic of dense overflow processes (a) during cooling and (b) after cooling is shut down. Numbers in blue circles will be used to reference different regions and processes in section 7.

shelf break, where the elevated minimum frequency renders them evanescent leading to interior reflection (Thomas and Wenegrat 2026). These waves then descend into a slantwise critical layer along the topography-aligned isopycnals (Fig. 8b, region 7), where their group velocity approaches zero and they are trapped and amplified (Qu et al. 2021b). Spectral peaks in the dissipation of kinetic energy at near-inertial frequencies, coincident with these reflection and trapping sites (Fig. 6b), mark where the waves are expected to break and mix.

These results also bear on how banded features in the interior of dense overflows should be interpreted. Along-isopycnal bands of shear and PV in the same region of earlier overflow

simulations were attributed to SI (Yankovsky and Legg 2019). The companion paper (Whitley et al. 2026) shows that the bottom injection of PV leaves this interior symmetrically stable, ruling out an SI origin for the bands here; the present analysis supplies an alternative explanation. The banded shear carries distinct near-inertial frequency peaks (Fig. 6a) and traces the ray paths of NIWs refracted by the overflow's PV structure and sloping isopycnals (Fig. 5), identifying it as the signature of propagating and trapped NIWs. Because SI and NIWs can leave visually similar slantwise imprints on the velocity field, discerning them calls for resolving the frequency content of the bands or diagnosing the interior PV directly—a distinction relevant to any overflow setting in which such features arise.

Earlier work with larger-scale, realistic overflow models has documented internal-wave generation by dense overflows and shown that capturing the wave field requires non-hydrostatic dynamics, but did not examine the near-inertial band in detail (Magaldi and Haine 2015). Here the overflow supplies its own near-inertial field, which is weak compared with the storm- and tide-forced waves of real high-latitude overflows (Alford et al. 2016; Kunze et al. 2023; Voet et al. 2024). The dissipation diagnosed should therefore be read as an artificially weak proxy for the real ocean. Even so, the intensification of near-inertial dissipation at the reflection and trapping sites is consistent with the enhanced mixing found beneath other sloping boundary currents (Qu et al. 2021b, 2022). A similar sequence has been observed in the Straits of Florida, where storm-generated NIWs reflect from the eastern side of the strait and become trapped and amplified where the isopycnals blanket the western side, driving bottom mixing (Qu et al. 2021a). There, the topography-aligned isopycnals are attributed to upslope Ekman arrest, whereas here they are established by the overflow itself, through the injection and advection of high PV by the gravity current and the resulting baroclinicity. These interactions are also unlikely to be captured in mesoscale-resolving models. While the storm- and tide-forced NIWs would be present in such models (Arbic et al. 2010; Barkan et al. 2021), they would not resolve the baroclinic and boundary-layer processes that generate the PV structure redirecting the waves seen here (e.g., Maltrud and McClean 2005; Legg et al. 2009; Danabasoglu et al. 2010; Colombo et al. 2020), and the reflection and trapping would likely be lost with them.

Quantifying the mixing these interactions drive will require examining these processes in the context of a realistic near-inertial wave field and measuring the resulting diapycnal fluxes and water-

mass transformation. This would show where along overflow pathways the wave–PV interaction matters most, and could inform parameterizations of near-boundary mixing. More generally, wherever a bottom-intensified current drapes its isopycnals over sloping topography and imprints a comparable PV structure, NIWs may be reflected and trapped, as they are here. The boundary processes that build that structure are then tied directly to mixing along the deep western boundary currents, and to the transformation of the newly formed dense water they carry into the global overturning circulation.

Acknowledgments. This material is based upon work supported by the National Science Foundation under Grants OCE-2232441, OCE-2342990, and OCE-2342991. We would like to acknowledge computing support from the Casper system (https://ncar.pub/casper) provided by the NSF National Center for Atmospheric Research (NCAR), sponsored by the National Science Foundation.

Data availability statement. Model configuration and analysis scripts will be publicly available at https://github.com/whitleyv/DenseOverflow.

References

Alford, M. H., J. A. MacKinnon, H. L. Simmons, and J. D. Nash, 2016: Near-inertial internal gravity waves in the ocean. *Annual Review of Marine Science*, **8**, 95–123, https://doi.org/10.1146/annurev-marine-010814-015746.

Arbic, B. K., A. J. Wallcraft, and E. J. Metzger, 2010: Concurrent simulation of the eddying general circulation and tides in a global ocean model. *Ocean Modelling*, **32**, 175–187, https://doi.org/10.1016/j.ocemod.2010.01.007.

Barkan, R., K. Srinivasan, L. Yang, J. C. McWilliams, J. Gula, and C. Vic, 2021: Oceanic mesoscale eddy depletion catalyzed by internal waves. *Geophysical Research Letters*, **48**, https://doi.org/10.1029/2021GL094376.

Buijsman, M. C., and Coauthors, 2026: A multiagency experiment on internal wave energy, mixing, and interactions and their representation in global ocean models and operational forecasts. *Bulletin of the American Meteorological Society*, **107 (1)**, E158 – E182, https://doi.org/10.1175/BAMS-D-24-0174.1.

Chalamalla, V. K., B. Gayen, A. Scotti, and S. Sarkar, 2013: Turbulence during the reflection of internal gravity waves at critical and near-critical slopes. *Journal of Fluid Mechanics*, **729**, 47–68, https://doi.org/10.1017/jfm.2013.240.

Colombo, P., and Coauthors, 2020: Representation of the denmark strait overflow in a z -coordinate eddying configuration of the nemo (v3.6) ocean model: resolution and parameter impacts. *Geoscientific Model Development*, **13**, 3347–3371, https://doi.org/10.5194/gmd-13-3347-2020.

Danabasoglu, G., W. G. Large, and B. P. Briegleb, 2010: Climate impacts of parameterized nordic sea overflows. *Journal of Geophysical Research: Oceans*, **115**, https://doi.org/10.1029/2010JC006243.

Eriksen, C. C., 1985: Implications of ocean bottom reflection for internal wave spectra and mixing. *Journal of Physical Oceanography*, **15**, 1145–1156, https://doi.org/10.1175/1520-0485(1985)015%3C1145:IOOBRF%3E2.0.CO;2.

Ferrari, R., A. Mashayek, T. J. McDougall, M. Nikurashin, and J.-M. Campin, 2016: Turning ocean mixing upside down. *Journal of Physical Oceanography*, **46**, 2239–2261, https://doi.org/10.1175/JPO-D-15-0244.1.

Girton, J. B., and T. B. Sanford, 2003: Descent and modification of the overflow plume in the denmark strait *. *Journal of Physical Oceanography*, **33**, 1351–1364, https://doi.org/GirtonSanford2003.

Kunze, E., 1985: Near-inertial wave propagation in geostrophic shear. *Journal of Physical Oceanography*, **15**, 544–565.

Kunze, E., R.-C. Lien, C. B. Whalen, J. B. Girton, B. Ma, and M. C. Buijsman, 2023: Seasonal variability of near-inertial/semidiurnal fluctuations and turbulence in the subarctic north atlantic. *Journal of Physical Oceanography*, **53**, 2717–2735, https://doi.org/10.1175/JPO-D-22-0231.1.

Kunze, E., C. Mackay, E. E. McPhee-Shaw, K. Morrice, J. B. Girton, and S. R. Terker, 2012: Turbulent mixing and exchange with interior waters on sloping boundaries. *Journal of Physical Oceanography*, **42**, 910–927, https://doi.org/10.1175/JPO-D-11-075.1.

Lamb, K. G., 2014: Internal wave breaking and dissipation mechanisms on the continental slope/shelf. *Annual Review of Fluid Mechanics*, **46**, 231–254, https://doi.org/10.1146/annurev-fluid-011212-140701.

Legg, S., and Coauthors, 2009: Improving oceanic overflow representation in climate models: The gravity current entrainment climate process team. *Bulletin of the American Meteorological Society*, **90**, https://doi.org/10.1175/2008BAMS2667.I.

Magaldi, M. G., and T. W. Haine, 2015: Hydrostatic and non-hydrostatic simulations of dense waters cascading off a shelf: The east greenland case. *Deep-Sea Research Part I: Oceanographic Research Papers*, **96**, 89–104, https://doi.org/10.1016/j.dsr.2014.10.008.

Magaldi, M. G., T. W. N. Haine, and R. S. Pickart, 2011: On the nature and variability of the east greenland spill jet: A case study in summer 2003*. *Journal of Physical Oceanography*, **41**, https://doi.org/10.1175/JPO-D-10.

Maltrud, M. E., and J. L. McClean, 2005: An eddy resolving global 1/10° ocean simulation. *Ocean Modelling*, **8**, 31–54, https://doi.org/10.1016/j.ocemod.2003.12.001.

Mooers, C. N. K., 1975: Several effects of a baroclinic current on the cross-stream propagation of inertial-internal waves†. *Geophysical Fluid Dynamics*, **6**, 245–275, https://doi.org/10.1080/03091927509365797.

Nokes, R. L., and G. N. Ivey, 1989: Vertical mixing due to the breaking of critical internal waves on sloping boundaries. *Journal of Fluid Mechanics*, **204**, 479–500, https://doi.org/10.1017/S0022112089001849.

Polzin, K. L., J. M. Toole, J. R. Ledwell, and R. W. Schmitt, 1997: Spatial variability of turbulent mixing in the abyssal ocean. *Science*, **276**, 93–96, https://doi.org/10.1126/science.276.5309.93.

Qu, L., L. Thomas, and J. Gula, 2021a: Bottom mixing enhanced by tropical storm-generated near-inertial waves entering critical layers in the straits of florida. *Geophysical Research Letters*, **48**, https://doi.org/10.1029/2021GL093773.

Qu, L., L. N. Thomas, and R. D. Hetland, 2021b: Near-inertial-wave critical layers over sloping bathymetry. *Journal of Physical Oceanography*, **51**, 1737–1756, https://doi.org/10.1175/JPO-D-20-0221.1.

Qu, L., L. N. Thomas, R. D. Hetland, and D. Kobashi, 2022: Mixing driven by critical reflection of near-inertial waves over the texas-louisiana shelf. *Journal of Physical Oceanography*, https://doi.org/10.1175/JPO-D-22-0004.1.

Remmler, S., S. Hickel, M. D. Fruman, and U. Achatz, 2015: Validation of large-eddy simulation methods for gravity wave breaking. *Journal of the Atmospheric Sciences*, **72**, 3537–3562, https://doi.org/10.1175/JAS-D-14-0321.1.

Slinn, D. N., and J. J. Riley, 1998: Turbulent dynamics of a critically reflecting internal gravity wave. *Theoretical and Computational Fluid Dynamics*, **11**, 281–303, https://doi.org/10.1007/s001620050094.

Smith, P. C., 1976: Baroclinic instability in the denmark strait overflow. *Journal of Physical Oceanography*, **6**, 355–371, https://doi.org/10.1175/1520-0485(1976)006⟨0355:BIITDS⟩2.0.CO;2.

Spall, M. A., R. S. Pickart, P. Lin, W.-J. von Appen, D. Mastropole, H. Valdimarsson, T. W. N. Haine, and M. Almansi, 2019: Frontogenesis and variability in denmark strait and its influence on overflow water. *Journal of Physical Oceanography*, **49**, 1889–1904, https://doi.org/10.1175/JPO-D-19-0053.1.

Taylor, J. R., and R. Ferrari, 2009: On the equilibration of a symmetrically unstable front via a secondary shear instability. *Journal of Fluid Mechanics*, **622**, 103–113, https://doi.org/10.1017/S0022112008005272.

Thomas, L. N., and J. O. Wenegrat, 2026: Interaction of internal waves with cyclonic flow in bottom boundary layers, manuscript in preparation.

Thorpe, A. J., and R. Rotuno, 1989: Nonlinear aspects of symmetric instability. *J. Atmos. Sci.*, **46**, 1285–1299, https://doi.org/10.1175/1520-0469(1989)046⟨1285:NAOSI⟩2.0.CO;2.

Voet, G., and Coauthors, 2024: Near-inertial energy variability in a strong mesoscale eddy field in the iceland basin. *Oceanography*, https://doi.org/10.5670/oceanog.2024.302.

Wagner, G. L., and Coauthors, 2025: High-level, high-resolution ocean modeling at all scales with oceananigans. *arXiv preprint (JAMES tbd)*.

Whitehead, J. A., M. E. Stern, G. R. Flierl, and B. A. Klinger, 1990: Experimental observations of baroclinic eddies on a sloping bottom. *Journal of Geophysical Research: Oceans*, **95**, 9585–9610, https://doi.org/10.1029/JC095iC06p09585.

Whitley, V., and J. Wenegrat, 2025: Breaking internal waves on sloping topography: Connecting parcel displacements to overturn size, interior–boundary exchanges, and mixing. *Journal of Physical Oceanography*, **55**, 645–661, https://doi.org/10.1175/JPO-D-24-0052.1.

Whitley, V., J. Wenegrat, and L. Thomas, 2026: Submesoscale dynamics of dense overflows. Part I: Potential vorticity fluxes and symmetric instability, Journal of Physical Oceanography, submitted.

Whitt, D. B., and L. N. Thomas, 2013: Near-inertial waves in strongly baroclinic currents. *Journal of Physical Oceanography*, **43**, 706–725, https://doi.org/10.1175/JPO-D-12-0132.1.

Yankovsky, E., and S. Legg, 2019: Symmetric and baroclinic instability in dense shelf overflows. *Journal of Physical Oceanography*, **49**, 39–61, https://doi.org/10.1175/JPO-D-18-0072.1.